

Interlayer-Exciton Based Nonvolatile Valleytronic Memory

Tong Ye¹, Yongzhuo Li^{3,4}, Junze Li¹, Hongzhi Shen¹, Junwen Ren¹, Cun-Zheng

Ning^{3,4,5}, Dehui Li^{1,2}*

¹School of Optical and Electronic Information, Huazhong University of Science and Technology, Wuhan 430074, China.

²Wuhan National Laboratory for Optoelectronics, Huazhong University of Science and Technology, Wuhan 430074, China.

³Department of Electronic Engineering, Tsinghua University, 100084 Beijing, China.

⁴Frontier Science Center for Quantum Information, 100084 Beijing, China.

⁵School of Electrical, Computer, and Energy Engineering, Arizona State University, Tempe, AZ 85287, USA.

Analogous to conventional charge-based electronics, valleytronics aims at encoding data via the valley degree of freedom, enabling new routes for information processing. Long-lived interlayer excitons (IXs) in van der Waals heterostructures (HSs) stacked by transition metal dichalcogenides (TMDs) carry valley-polarized information and thus could find promising applications in valleytronic devices. Although great progress of studies on valleytronic devices has been achieved, nonvolatile valleytronic memory, an indispensable device in

valleytronics, is still lacking up to date. Here, we demonstrate an IX-based nonvolatile valleytronic memory in a WS₂/WSe₂ HS. In this device, the emission characteristics of IXs exhibit a large excitonic/valleytronic hysteresis upon cyclic-voltage sweeping, which is ascribed to the chemical-doping of O₂/H₂O redox couple trapped between the TMDs and substrate. Taking advantage of the large hysteresis, the first nonvolatile valleytronic memory has been successfully made, which shows a good performance with retention time exceeding 60 minutes. These findings open up an avenue for nonvolatile valleytronic memory and could stimulate more investigations on valleytronic devices.

Van der Waals HSs stacked by TMDs monolayers enable the generation of long-lived IXs with a large binding energy of about 150 meV¹, and a long diffusion distance over five micrometres², further extending the already appealing properties of the constituent TMDs monolayers. Since IXs are composed of electrons and holes that are resided in neighboring layers, their physical properties strongly depend on the layer configurations and external fields or dopings^{3,4}. Through electrical field or doping, we can modulate the emission intensity and wavelength of the IXs¹, and even switch its polarization⁵. Recently, IXs in the HSs stacked by other layered materials such as 2D perovskites and InSe with TMDs monolayer have been demonstrated and can be utilized in mid-infrared photodetections^{6,7}.

In particular, IXs in TMDs-based heterostructures carry valley-polarized information and thus would find promising applications in valleytronics taking advantage of their long lifetime⁸. Previous studies have demonstrated that IXs exhibit

a large valley-polarization degree that can be tuned in a wide range by external electric field⁹ and magnetic field¹⁰. Although considerable progress has been made in valleytronics, nonvolatile valleytronic memory has not been achieved up to date, which is indispensable for valleytronic devices. To this end, it is urgent to explore possible strategies to efficiently store valley-polarized information for further development of valleytronic devices and chips. Here, we have successfully achieved an IX-based nonvolatile valleytronic memory, which would greatly prompt relevant investigations on valleytronics.

In this work, the HS device is formed by a monolayer WS₂ (top) and a monolayer WSe₂ (bottom), both of which are contacted with an electrode (Fig. 1a). By applying voltage between the electrode and the heavily-doped Si substrate, we can control the doping level of the device when performing optical measurements. Figure 1b shows the optical microscope image of the device. The WS₂ and WSe₂ sheets are mechanically exfoliated from their respective bulk crystals and then transferred on a SiO₂/p⁺⁺-Si substrate through dry-transfer technique¹¹. The edges of the two sheets are intentionally aligned to improve interlayer coupling³.

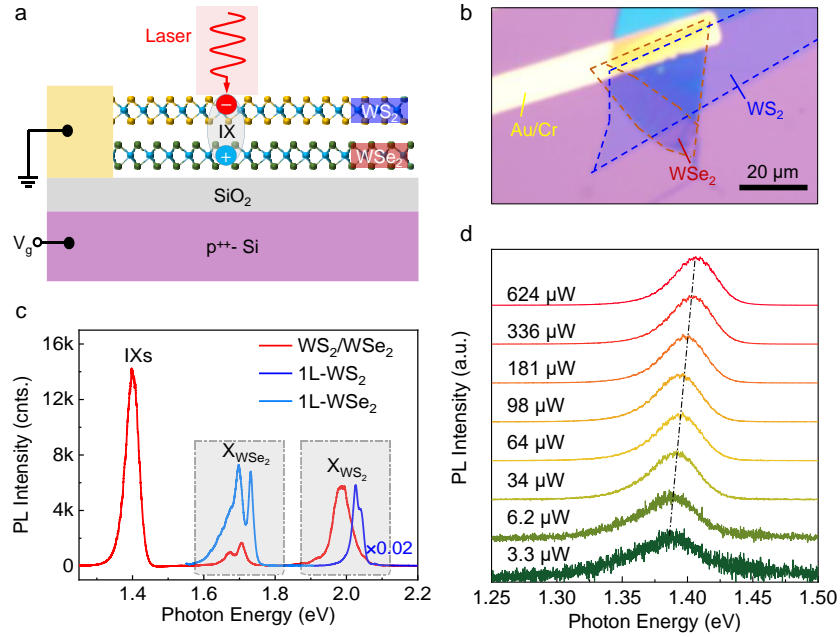


Fig. 1|IXs in a WS₂/WSe₂ HS. **a-b**, Schematic and optical microscope image of the device, respectively. **c**, PL spectra of the HS and monolayer WSe₂ and WS₂. For a clear visualization, the PL spectrum of individual WS₂ is multiplied by a factor 0.02. **d**, PL spectra of the IXs as a function of excitation power. The spectra are vertically shifted for clarity. The sample was excited by a 532 nm laser with a power of 23 μ W at 78 K.

IXs in the WS₂/WSe₂ HS. Fig. 1c shows the PL spectra of the HS, from which we can observe severe PL quenching and redshift of the intralayer excitonic peaks, together with the appearance of a low-energy peak at 1.4 eV. The quenching and redshift of the intralayer excitonic peaks can be attributed to interlayer charge transfer^{12,13} and modified dielectric environment^{14,15}, respectively. We ascribe the peak at 1.4 eV to the IX emission according to previous reports^{16,17}. The excitation-power dependent PL spectra further verify its interlayer nature (Fig. 1d). The IX emission peak shows a blueshift with the increase of excitation power, which is due to many-body effect arising

from the repulsive interaction between the dipole-aligned IXs^{4,18,19}.

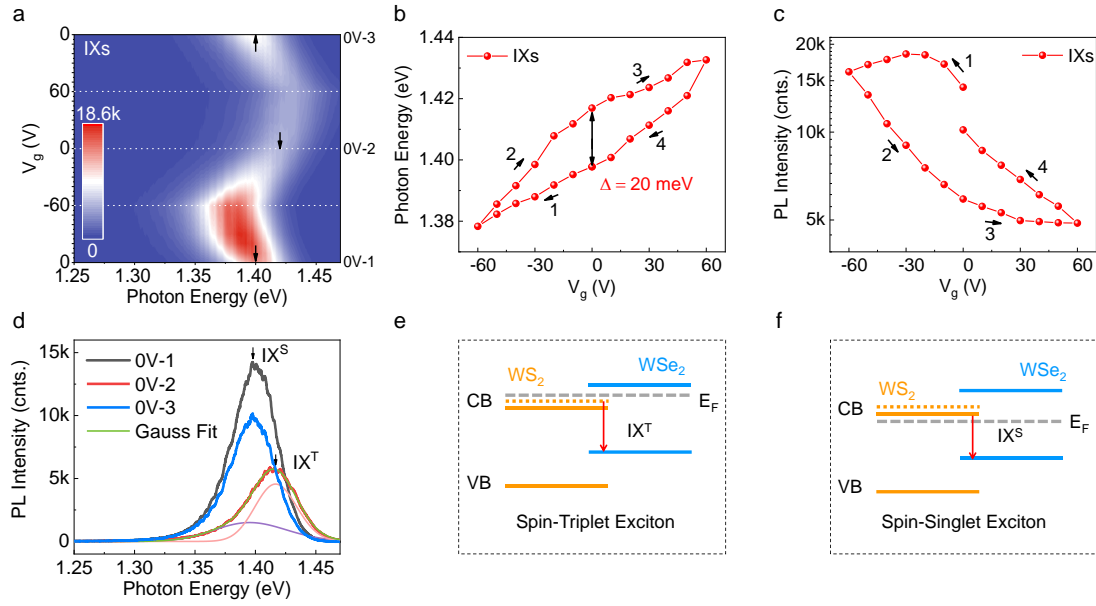


Fig. 2 | Electrical control of the IX emission. **a**, Contour plot for the PL spectra of IXs upon cyclic V_g . The white dashed lines serve as guides to the eye. Black arrows mark the peak positions of the IXs at 0 V with different scanning sequences. **b-c**, Photon energy and PL intensity of the IX emission as a function of V_g . **d**, PL spectra of the IXs at 0 V with different scanning sequences. 0V-1, 0V-2 and 0V-3 represent three spectra marked in **a**. The 0V-2 spectrum is fitted by a Gaussian function. The sample was excited by a 532 nm laser with 23 μ W power at 78 K. **e-f**, Schematic of the spin-triplet and spin-singlet excitons. Chemical-doped electrons lift the Fermi level up and shift the IXs to the spin-triplet state (IX^T). When those electrons are released, the IXs return to the spin-singlet state (IX^S). The orange dashed line stands for the upper spin-splitting conduction band (CB) of WS_2 . Red arrows represent the recombination paths of the IXs.

Excitonic hysteresis of IXs. To explore gate-dependent features of the IX emission, we measured the PL spectra of the device under cyclic V_g , which scans first

from 0 V to -60 V, then 0 V all the way to 60 V and finally back to 0 V (Fig. 2a). The IX emission peak shows a redshift and the emission intensity is enhanced with the decrease of V_g , and vice versa. The redshift of the IX emission peak with V_g can be ascribed to the Stark effect^{5,20}, which is further verified by the opposite shift trend of the IX emission peak in devices with stacking order inversed (Fig. S1). Interestingly, the IX emission peak exhibits a strong hysteresis upon cyclic-voltage sweeping. As indicated by the black arrows in Fig. 2a, the peak energy of the IXs at middle 0 V (0V-2) cannot return to the same value of initial 0 V (0V-1), until a further upward scanning that is finally back to 0 V (0V-3). The gate-dependent photon energy and PL intensity can be seen more clearly in Fig. 2b and 2c. For a simple discussion, we only compare the states at 0V-2 and 0V-3. The photon energy of 0V-2 is blueshifted by about 20 meV with respect to that of 0V-3. Meanwhile, the PL intensity of 0V-2 is weaker than 0V-3 with a contrast ratio of about 1.7. It is worth to mention that the light intensity changes non-monotonously as V_g decreases from 0 V to -60 V, indicating the occurrence of chemical doping²¹⁻²³, which will be discussed in the following.

As shown in Fig. 2d, the IX emission peak of 0V-2 can be decomposed to two Gaussian peaks (detailed fittings of the spectra are provided in Fig. S2). The energy difference of the two peaks is about 20 meV, which is consistent with the splitting energy of the conduction band of WS₂^{24,25}, strongly suggesting the occurrence of spin-triplet excitons^{26,27}. This peculiar phenomenon can be understood from the chemical-doping^{21,22} induced band-filling effect^{5,28}, as depicted in Fig. 2e and 2f. When the device is chemically *n*-doped, the Fermi level will be lift up and IXs will shift to the spin-

triplet state (IX^T), which has an inefficient PL yield because of inverted spin. Contrarily, when the chemically-doped electrons are released, IXs will return to the spin-singlet state (IX^S). Therefore, the IX emission peaks in 0V-1 and 0V-3 spectra are attributed to IX^S emission, and that in 0V-2 spectra is mainly resulted from IX^T . The IX^T and IX^S peaks can be well resolved in PL spectra acquired by picosecond laser excitation (Fig. S3a). In addition, the intensity ratio of IX^T/IX^S increases with the increase of V_g (Fig. S3b), thus confirming the band-filling mechanism and IX^T/IX^S origins. We have also measured the gate-dependent lifetime of the IXs (Fig. S3, c-e). The lifetime of the IXs at 0V-2 is slightly shorter than at 0V-1 and 0V-3 rather than getting prolonged, further supporting the IX^T/IX^S origins¹⁰. The difference of light intensities between 0V-3 and 0V-1 might be due to different levels of chemical doping at the initial and final sweeping stages, as discussed in the following.

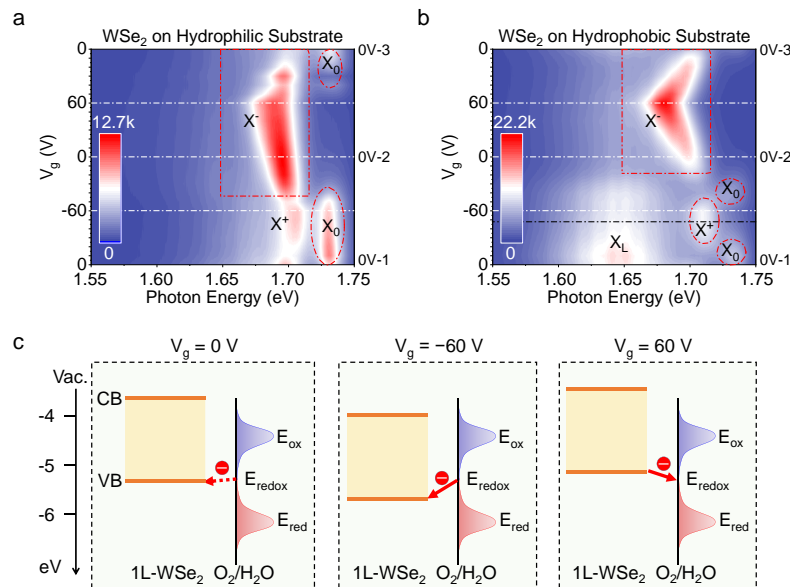


Fig. 3|Mechanism of the excitonic hysteresis. (a) Contour plot for the PL spectra of monolayer WSe₂ as a function of cyclic V_g . The spectra were acquired in the individual WSe₂ region of the HS on a hydrophilic substrate. **(b)** Contour plot for the PL spectra of

monolayer WSe₂ on a hydrophobic substrate, which is functionalized by hexamethyldisilazane (HMDS). The black dashed line indicates the symmetric position of the evolution tracks of X^+ and X_0 . The PL measurements were conducted at 78 K with 532 nm laser excitation (23 μ W). (c) Illustration of chemical doping caused by O₂/H₂O molecules. The electronic density of states (DOS) reflect the electron energy distribution around the oxidation potential (E_{ox}) and reduction potential (E_{red}), respectively.

Mechanism of the excitonic hysteresis. Electrical hysteresis has been observed in devices based on two-dimensional materials, such as graphene and TMDs based field-effect transistors^{29,30}. Generally, electrical hysteresis is attributed to the chemical-doping effect by doping species (O₂ and H₂O) that are bound at the device/substrate interface, and/or on the surface of the device³¹⁻³³. In our case, we propose that the excitonic hysteresis mentioned above is originated from the same scenario.

Since our measurements were performed in high vacuum ($\sim 10^{-7}$ Torr), the influence of the molecules on the device surface can be safely neglected. Therefore, the excitonic hysteresis is more likely due to the O₂/H₂O molecules that are trapped at the interface between the HS and substrate. To clarify this, we examine the gate-dependent PL spectra of the individual WSe₂ region (Fig. 3a), because WSe₂ is in the bottom of the HS and directly contacts the SiO₂/Si substrate. Additionally, we conducted a control experiment with WSe₂ monolayer on a hydrophobic substrate (Fig. 3b).

The emission features of the intralayer excitons in WSe₂ are closely correlated to

that of IXs. As V_g decreases from 0 V to -60 V, the emission of positive trions (X^+) is gradually enhanced, while the peak of neutral excitons (X_0) is suppressed, indicating an efficient hole doping (detailed data is provided in Fig. S4). Peculiarly, as V_g increases from -60 V back to 0 V, the evolution track is asymmetric to that from 0 V to -60 V. The trion emission peak is firstly weakened, then enhanced and redshifted with the increase of V_g . The asymmetric evolution strongly indicates the occurrence of negative trions (X^-), and suggests that the WSe₂ is chemically *n*-doped^{33,34} at 0V-2. When V_g increases from 0 V to 60 V, the X^- peak is redshifted further, but with emission intensity weakened because of Coulomb screening from the free electrons³⁵. When voltage scans backward from 60 V to 0 V, the X^- peak shows a blueshift and the emission intensity becomes weaker while the X_0 peak is gradually enhanced, indicating that the chemically-doped electrons have been released. All the above features are well consistent with the previously mentioned chemical-doping effect.

To further validate such hypothesis, we then focus on the PL spectra of a control device with monolayer WSe₂ on a hydrophobic substrate (Fig. 3b). The evolution tracks of X^+ and X_0 emission are roughly symmetrical along the black dashed line at about -50 V. The slight deviation of the symmetry line at -50 V (rather than -60 V) might be due to trace O₂/H₂O molecules that are adsorbed on WSe₂ before the transfer procedure. Besides, in sharp contrast to Fig. 3a, the track of X^- is quasi-symmetrical along the dashed line at 60 V, suggesting that the excitonic hysteresis is largely suppressed. Therefore, H₂O molecules should play a critical role in our observations. The broad PL peak centered at about 1.65 eV might be due to local-state exciton (X_L)³⁶, which is out of

the scope of this study.

The surface of SiO₂ is usually covered with a layer of silanol groups ($\equiv \text{Si} - \text{OH}$), especially after it is treated by piranha solution or plasma cleaner^{21,33}. With these silanol groups, SiO₂/Si substrates are easily bound by ambient O₂ and H₂O molecules³³. As shown in Fig. 3c, the electrochemical potential of the redox couple (O₂/H₂O) is about -5.3 eV ^{21,37}, which is slightly higher than the valence band of WSe₂ (about -5.46 eV)^{38,39}. Therefore, electrons spontaneously transfer from O₂/H₂O to WSe₂, making monolayer WSe₂ initially *n*-doped (detailed information is provided in Fig. S4), and resulting in the deviated symmetry at -50 V in Fig. 3b.

When applying negative gate voltages, electrons are forced to transfer further from O₂/H₂O to WSe₂. Consequently, the Fermi level of the HS is lifted up, and IXs shift to the spin-triplet state (Fig. 2e). Those chemically-doped electrons balance out the gate modulation, resulting in the non-monotonic behavior of the IXs in $0 \sim -60 \text{ V}$ range (Fig. 2c) and the excitonic hysteresis. The chemical-doping effect also explains why X_0 emission maintains its intensity from 0 V to -60 V for WSe₂ on the hydrophilic substrate (Fig. 3a) but greatly suppressed on the hydrophobic substrate (Fig. 3b).

When applying positive gate voltages, the chemical-doped electrons are driven back from WSe₂ to the O₂/H₂O redox couple. Therefore, IXs return to the spin-singlet state (Fig. 2f) when V_g scans back to 0V . This control experiment further verifies the chemical-doping mechanism and well explains the origin of the excitonic hysteresis of IXs shown in Fig. 2. We have made dozens of HSs on hydrophobic and hydrophilic substrates, and we can only observe excitonic hysteresis (both photon-energy and PL-

intensity hysteresis) in the samples on hydrophilic substrates. The hysteresis is largely suppressed in HSs stacked on hydrophobic substrates (Fig. S5). In addition, we have also fabricated a $\text{WS}_2/\text{WSe}_2/\text{hBN}$ HS on a hydrophilic substrate with WS_2/WSe_2 HS partially separated from the substrate by a thin layer hBN. For this device, the excitonic hysteresis is observed in the region where WS_2/WSe_2 HS directly contacts with the substrate, but absent in the hBN-insulated region (Fig. S6), further supporting the chemical-doping mechanism. The hysteretic behavior is well reproducible in multiple repeating measurements and also in different samples. Therefore, we rule out the influence of random contamination.

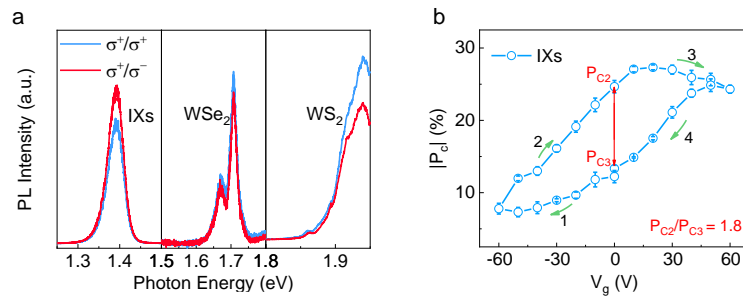


Fig. 4|Electrically-tunable valley polarization of the IXs. a, Helicity-resolved PL spectra of the HS under 633 nm excitation (180 μW) at 78 K. **b,** Absolute circular polarization degree of the IXs as a function of V_g . The helicity contrast is defined as P_{c2}/P_{c3} , where P_{c2} and P_{c3} is the absolute circular polarization degree of 0V-2 and 0V-3, respectively.

Valleytronic hysteresis of the IXs. To study the chemical-doping effect on the valley-polarized features of the IXs, we measured the helicity-resolved PL spectra of the device (Fig. 4a). Interestingly, the IX peak exhibits a negative circular polarization in contrast to that of intralayer excitons in WSe_2 and WS_2 , which can be ascribed to the

interlayer quantum interference imposed by the atomic registry between the constituent layers⁴⁰. To qualify the valley polarization, the degree of circular polarization (DOCP) has been introduced and defined as $P_c = (I^+ - I^-)/(I^+ + I^-)$, where I^+ (I^-) denotes the intensity of co-polarized (cross-polarized) PL component. For the IXs peak, $P_c = -12.3\%$, while for the intralayer excitonic peak of WS₂ and WSe₂, $P_c = 15\%$ and 7.1% , respectively.

The DOCP of the IXs can also be electrically controlled by V_g , as shown in Fig. 4b (the full data set is provided in Fig. S7). The absolute DOCP is greatly suppressed at -60 V (p -doping), but enhanced at 60 V (n -doping). This phenomenon has been reported by Scuri and coworkers, and is attributed to changes in valley-depolarization-time caused by electron/hole doping⁴¹. Similarly, we believe our observation can also ascribed to the charge doping from external applied bias and chemical doping (Fig. S3). Interestingly, the DOCP and lifetime (Fig. S3e) of the IXs also exhibit a strong hysteresis, probably due to the carrier trapping and detrapping induced by the above-mentioned chemical-doping, which leads to the different doping concentration and further different valley-depolarization-time and DOCP under the same gate voltage. To sum up, the chemical-doping effect leads to the formation of spin-triplet exciton, and gives rise to the hysteresis of excitonic emission, valley-polarization degree and lifetime of IXs, which could find potential applications in nonvolatile valleytronic information processing.

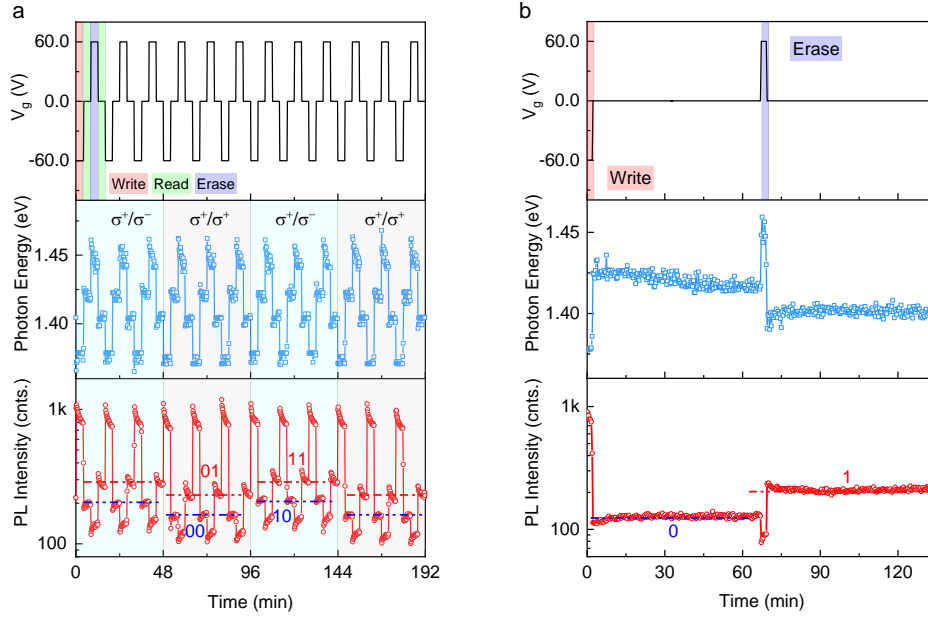


Fig. 5|Electrically controlled memory operation in the HS. a, Time-dependent IX emission characteristics upon cyclic V_g among -60 V, 0 V, 60 V and 0 V. Each voltage lasts for about 4 minutes. The detecting polarization shifts every three cycles of V_g . **b**, Retention time of the “1” and “0” excitonic states. The writing and erasing voltages last for about 3 minutes, and the reading voltage lasts for about 64 minutes. The peak energies and intensities are extracted from real-time spectra, each of which was measured within 10 s. The sample was excited by a 633 nm laser with a power of $180 \mu\text{W}$ at 78 K.

IX-based valleytronic memory. To demonstrate the valleytronic memory ability of the device, we measured time-dependent PL spectra under circular excitation (σ^+), as shown in Fig. 5a. As gate voltage cyclically changes among -60 V, 0 V, 60 V and 0 V, the photon energy of the IX emission periodically shifts among 1.38 eV, 1.42 eV, 1.45 eV and 1.40 eV, which are analogous to the performance of conventional electronic devices under “write”, “read” and “erase” operations. In addition, the

emission intensity also periodically changes in response to those memory operations. Specifically, the intensity level of IX^S (IX^T) located at 1.40 (1.42) eV can be regarded as digital information 1 (0), which can persist for a long time with no power consumption, suggesting potential applications in nonvolatile storage. Intriguingly, as the detection helicity switches between σ^- and σ^+ , the PL intensity of the 0 and 1 states exhibit helicity-resolved features. There are four intensity levels emerging, which can be defined as “00”, “01”, “10” and “11”, indicating valley-encoding abilities of the device. Based on this feature, we can selectively encode/address the valley-polarized information by helicity excitation/detection.

To evaluate the retention time of the encoded information, we then prolong the reading-operation time, as shown in Fig. 5b. Surprisingly, the 1 and 0 excitonic states can persist for at least 60 minutes, holding great promise for nonvolatile valleytronic memories. As a matter of fact, the retention time should be much longer than 60 minutes, as can be seen in a logarithmic-timescale plot (Fig. S8a). We also note that the 0 (1) state varies dynamically before reaching a steady state. This is probably due to the charging/discharging process of the device, as confirmed by the features of time-dependent leakage current (Fig. S8b). It is worth to mention that the information encoding ability of the device can persist up to 250 K, which is promising for high temperature valleytronic applications (Fig. S9).

Since the nonvolatile valleytronic memory has never been reported, it is hard to make an objective comparison. Nevertheless, the device is similar to photonic memory, thus we list the parameters of our device and other nonvolatile photonic memories in

Table 1, which shows that our device is outperforming in comparison with peer memory devices. The PL ON/OFF ratio of the 1/0 states could be as large as 3.6 (Fig. S10), which is larger than peer photonic memories⁴²⁻⁴⁵. The power consumption of the device is estimated to be about 74/56 nW for set/reset operation (Fig. S8b), which is extremely low in comparison with other phase-change photonic memories⁴²⁻⁴⁵. The switching time of our devices could be very short but limited by our testing system, since the hysteresis effect could be established in several microseconds according to previous reports⁴⁶.

Table 1. Parameters of our device and peer works. The abbreviations of ele-photonic, E.P. and O.P. stand for electrical-photonic, electrical programing, and optical programing, respectively.

Memory Type	ON/OFF Ratio	Operation Time (ns)	Power(Set/Reset) (mW)	Ref.
all-photonic	1.21	1	53.3 (O.P.)	[⁴²]
all-photonic	1.8	5	10/30 (O.P.)	[⁴⁵]
ele-photonic	3.16	80100	10/110 (E.P.)	[⁴³]
ele-photonic	1.04	510 (E.P.) 408 (O.P.)	0.03/1.2 (E.P.) 7.5 (O.P.)	[⁴⁴]
ele-photonic	3.6	--	74/56 *10⁻⁶ (E.P.)	This work

CONCLUSIONS

In summary, we have systematically investigated the excitonic/valleytronic hysteresis of IXs in a WS₂/WSe₂ HS. By examining the PL spectra of the WSe₂ monolayers on hydrophilic and hydrophobic substrates, we verify that the origin of the

hysteresis is the chemical-doping of WSe₂ by O₂/H₂O redox couple. Benefiting from the hysteresis effect, IXs can be electrically switched between a spin-singlet state and a spin-triplet state, enabling the applications in valleytronic information processing. Finally, we demonstrate the memory function of the device, which shows a good writing/reading/erasing ability with retention time exceeding 60 minutes. Our study provides a potential paradigm to achieve nonvolatile valleytronic memory and thus would greatly advance the development of valleytronic devices.

METHODS

Sample Preparations. Electrodes were fabricated by standard photolithography and thermal evaporation (50 nm/2 nm Au/Cr). The substrates with prefabricated electrodes are ultrasonic cleaned and plasma cleaned before the fabrication of the HS. WS₂ and WSe₂ monolayer flakes were first mechanically exfoliated onto polymethylmethacrylate (PMMA) stamps, and then transferred on a SiO₂ (300 nm)/Si wafer using a dry transfer technique with the aid of an optical microscope and a nano-manipulator. The hydrophobic substrates were prepared via immersing in HMDS vapor for 10 min and then rinsing with acetone for 30 s to form a hydrophobic layer on the substrate⁴⁷. All the samples are not treated by thermal annealing, because the thermal-annealing procedure can disable or deteriorate the performance of nonvolatile memory devices.

Optical Measurements. The as-fabricated devices were mounted in a continuous flow cryostat with 10⁻⁷ Torr vacuum. For gate-dependent PL measurement, the sample was excited by a 532 nm laser (23 μW) at 78 K. For the helicity-resolved PL measurement, the sample was excited by a 633 nm laser with a power of 180 μW at 78 K. The time

interval between two adjacent spectra is about 1 minute when performing gate-dependent measurement. For the memory operation measurement, the spectra were acquired with V_g changing cyclically and laser keeping focused on the sample. Each spectrum was measured within 10 seconds. All the PL spectra were collected by a 50 \times objective lens (N.A. = 0.7) in a Raman spectrometer (Horiba HR550) with a 600 g/mm grating. A Keithley 2400 sourcemeter was used as the voltage source.

ASSOCIATED CONTENT

Supporting Information

The supporting information consists of: 1) Gate-dependent PL spectra for a stacking-order inversed HS (WSe₂/WS₂) on a hydrophilic substrate; 2) Lorentz and Gaussian fittings of 0V-1, V-2 and 0V-3 spectra; 3) Spin-singlet and spin-triplet IXs and their lifetimes; 4) PL spectra of the WSe₂ monolayer under gate voltages from 0 V to -60 V shown in Fig. 3a; 5) Gate-dependent PL spectra for a WS₂/WSe₂ HS on a hydrophobic substrate; 6) Gate-dependent PL spectra of a WS₂/WSe₂/hBN HS; 7) Helicity-resolved PL spectra of the WS₂/WSe₂ HS; 8) Electrically controlled memory operation in the HS; 9) Memory performance of the WS₂/WSe₂ HS under different temperatures; 10) PL spectra of 0V-2 and 0V-3 states and the ON/OFF intensity Ratio.

AUTHOR INFORMATION

Corresponding Author

*E-mail: dehuili@hust.edu.cn.

Notes

The authors declare no competing financial interest.

ACKNOWLEDGMENT

D. L. acknowledges the support from National Key Research and Development Program of China (2018YFA0704403), NSFC (62074064) and Innovation Fund of WNLO. T. Y. gratefully acknowledges, Jian Zhang, Danyang Zhang and Jiaqi Wang for the help in conducting experiments.

REFERENCES

- 1 Jauregui, L. A. *et al.* Electrical control of interlayer exciton dynamics in atomically thin heterostructures. *Science* **366**, 870 (2019).
- 2 Unuchek, D. *et al.* Room-temperature electrical control of exciton flux in a van der Waals heterostructure. *Nature* **560**, 340 (2018).
- 3 Nayak, P. K. *et al.* Probing Evolution of Twist-Angle-Dependent Interlayer Excitons in MoSe₂/WSe₂ van der Waals Heterostructures. *ACS Nano* **11**, 4041 (2017).
- 4 Rivera, P. *et al.* Observation of long-lived interlayer excitons in monolayer MoSe₂-WSe₂ heterostructures. *Nat. Commun.* **6**, 6242 (2015).
- 5 Ciarrocchi, A. *et al.* Polarization switching and electrical control of interlayer excitons in two-dimensional van der Waals heterostructures. *Nat. Photonics* **13**, 131 (2019).

- 6 Ubrig, N. *et al.* Design of van der Waals interfaces for broad-spectrum optoelectronics. *Nat. Mater.* **19**, 299 (2020).
- 7 Chen, Y. *et al.* Robust Interlayer Coupling in Two-Dimensional Perovskite/Monolayer Transition Metal Dichalcogenide Heterostructures. *ACS Nano.* **14**, 8, 10258–10264 (2020).
- 8 Rivera, P. *et al.* Interlayer valley excitons in heterobilayers of transition metal dichalcogenides. *Nat. Nanotechnol.* **13**, 1004 (2018).
- 9 Rivera, P. *et al.* Valley-polarized exciton dynamics in a 2D semiconductor heterostructure. *Science* **351**, 688-691 (2016).
- 10 Jiang, C. *et al.* Microsecond dark-exciton valley polarization memory in two-dimensional heterostructures. *Nat. Commun.* **9**, 753 (2018).
- 11 Castellanos-Gomez, A. *et al.* Deterministic transfer of two-dimensional materials by all-dry viscoelastic stamping. *2D Mater.* **1**, 011002 (2014).
- 12 Jin, C. *et al.* Ultrafast dynamics in van der Waals heterostructures. *Nat. Nanotechnol.* **13**, 994 (2018).
- 13 Hong, X. *et al.* Ultrafast charge transfer in atomically thin MoS₂/WS₂ heterostructures. *Nat. Nanotechnol.* **9**, 682 (2014).
- 14 Kumar, R. *et al.* Interlayer screening effects in WS₂/WSe₂ van der Waals hetero-bilayer. *2D Mater.* **5**, 041003 (2018).
- 15 Raja, A. *et al.* Coulomb engineering of the bandgap and excitons in two-dimensional materials. *Nat. Commun.* **8**, 15251 (2017).
- 16 Jin, C. *et al.* Identification of spin, valley and moiré quasi-angular momentum

- of interlayer excitons. *Nat. Phys.* **15**, 1140 (2019).
- 17 Ye, T. *et al.* Charge-Accumulation Effect in Transition Metal Dichalcogenide Heterobilayers. *Small* **15**, 1902424 (2019).
- 18 Butov, L. V. *et al.* Towards Bose–Einstein condensation of excitons in potential traps. *Nature* **417**, 47 (2002).
- 19 Nagler, P. *et al.* Interlayer exciton dynamics in a dichalcogenide monolayer heterostructure. *2D Mater.* **4**, 025112 (2017).
- 20 Wang, T. *et al.* Giant Valley-Zeeman Splitting from Spin-Singlet and Spin-Triplet Interlayer Excitons in WSe₂/MoSe₂ Heterostructure. *Nano Lett.* **20**, 694 (2020).
- 21 Xu, H. *et al.* Investigating the mechanism of hysteresis effect in graphene electrical field device fabricated on SiO₂ substrates using Raman spectroscopy. *Small* **8**, 2833 (2012).
- 22 Liu, H. *et al.* Two-Dimensional WSe₂/Organic Acceptor Hybrid Nonvolatile Memory Devices Based on Interface Charge Trapping. *ACS Appl. Mater. Interfaces* **11**, 34424 (2019).
- 23 Ye, T. *et al.* Room-Temperature Exciton-Based Optoelectronic Switch. *Small*, e2005918 (2021).
- 24 Echeverry, J. P. *et al.* Splitting between bright and dark excitons in transition metal dichalcogenide monolayers. *Phys. Rev. B* **93**, 121107 (2016).
- 25 Eickholt, P. *et al.* Spin Structure of K Valleys in Single-Layer WS₂ on Au(111). *Phys Rev Lett* **121**, 136402 (2018).

- 26 Yu, H. *et al.* Brightened spin-triplet interlayer excitons and optical selection rules in van der Waals heterobilayers. *2D Mater.* **5**, 035021 (2018).
- 27 Andrew Y. Joe. *et al.* Electrically controlled emission from triplet charged excitons in atomically thin heterostructures. *arXiv:2012.04022* (2020).
- 28 Jones, A. M. *et al.* Spin–layer locking effects in optical orientation of exciton spin in bilayer WSe₂. *Nat. Phys.* **10**, 130 (2014).
- 29 Ye, T. *et al.* Approaching the Intrinsic Lifetime and Modulating a Graphene Plasmonic Resonance at a Few Hundred GHz. *Adv. Opt. Mater.* **7**, 1900315 (2019).
- 30 Urban, F. *et al.* Gas dependent hysteresis in MoS₂ field effect transistors. *2D Mater.* **6**, 045049 (2019).
- 31 Shu, J. *et al.* The intrinsic origin of hysteresis in MoS₂ field effect transistors. *Nanoscale* **8**, 3049 (2016).
- 32 Kaushik, N. *et al.* Reversible hysteresis inversion in MoS₂ field effect transistors. *npj 2D Mater. Appl.* **1**, 34 (2017).
- 33 Park, K. *et al.* Redox-governed charge doping dictated by interfacial diffusion in two-dimensional materials. *Nat. Commun.* **10**, 4931 (2019).
- 34 Zheng, L. *et al.* Reversible n-Type Doping of Graphene by H₂O-Based Atomic-Layer Deposition and Its Doping Mechanism. *J. Phys. Chem. C* **119**, 5995 (2015).
- 35 Chernikov, A. *et al.* Electrical Tuning of Exciton Binding Energies in Monolayer WS₂. *Phys. Rev. Lett.* **115**, 126802 (2015).

- 36 Shang, J. *et al.* Observation of Excitonic Fine Structure in a 2D Transition-Metal Dichalcogenide Semiconductor. *ACS Nano* **9**, 647-655 (2015).
- 37 Chakrapani, V. *et al.* Charge Transfer Equilibria Between Diamond and an Aqueous Oxygen Electrochemical Redox Couple. *Science* **318**, 1424 (2007).
- 38 Wang, K. *et al.* Electrical control of charged carriers and excitons in atomically thin materials. *Nat. Nanotechnol.* **13**, 128 (2018).
- 39 Li, X. *et al.* Graphene and related two-dimensional materials: Structure-property relationships for electronics and optoelectronics. *Appl. Phys. Rev.* **4**, 021306 (2017).
- 40 Hsu, W. T. *et al.* Negative circular polarization emissions from WSe₂/MoSe₂ commensurate heterobilayers. *Nat. Commun.* **9**, 1356 (2018).
- 41 Scuri, G. *et al.* Electrically Tunable Valley Dynamics in Twisted WSe₂/WSe₂ Bilayers. *Phys. Rev. Lett.* **124**, 217403 (2020).
- 42 Ríos, C. *et al.* Integrated all-photonic non-volatile multi-level memory. *Nat. Photonics* **9**, 725-732 (2015).
- 43 Zheng, J. *et al.* Nonvolatile Electrically Reconfigurable Integrated Photonic Switch Enabled by a Silicon PIN Diode Heater. *Adv. Mater.* **32**, 2001218 (2020).
- 44 Farmakidis, N. *et al.* Plasmonic nanogap enhanced phase-change devices with dual electrical-optical functionality. *Sci. Adv.* **5**, eaaw2687 (2019).
- 45 Arjunan, M. S. *et al.* High-Stability and Low-Noise Multilevel Switching in In₃SbTe₂ Material for Phase Change Photonic Memory Applications. *Phys. Status Solidi RRL*, 2000354 (2020).

- 46 Datye, I. M. *et al.* Reduction of hysteresis in MoS₂ transistors using pulsed voltage measurements. *2D Mater.* **6**, 011004 (2018).
- 47 Li, L. *et al.* Two-Step Growth of 2D Organic-Inorganic Perovskite Microplates and Arrays for Functional Optoelectronics. *J Phys. Chem. Lett.* **9**, 4532 (2018).